

## Understanding the deficiency in inertial confinement fusion hohlraum x-ray flux predictions using experiments at the National Ignition Facility

Hui Chen , D. T. Woods , W. A. Farmer , N. A. Aybar , D. A. Liedahl, S. A. MacLaren , M. B. Schneider , H. A. Scott , D. E. Hinkel, O. L. Landen , J. D. Moody, M. D. Rosen , J. S. Ross , S. Rogers, N. Roskopf , G. F. Swadling , and S. Vohnhof

*Lawrence Livermore National Laboratory, Livermore, California 94550, USA*

 (Received 16 April 2024; accepted 20 June 2024; published 15 July 2024)

The predicted implosion performance of deuterium-tritium fuel capsules in indirect-drive inertial confinement fusion experiments relies on precise calculations of the x-ray drive in laser-heated cavities (hohlraums). This requires accurate, spectrally dependent simulations of laser to x-ray conversion efficiencies and x-ray absorption losses to the hohlraum wall. A set of National Ignition Facility experiments have identified a cause for the long-standing hohlraum “drive deficit” as the overprediction of gold emission at  $\sim 2.5$  keV in nonlocal thermodynamic equilibrium coronal plasma regions within the hohlraum. Reducing the emission and absorption opacity in this spectral region by  $\sim 20\%$  brings simulations into agreement with measured x-ray fluxes and spectra.

DOI: [10.1103/PhysRevE.110.L013201](https://doi.org/10.1103/PhysRevE.110.L013201)

In indirect-drive inertial confinement fusion (ICF) experiments at the National Ignition Facility (NIF) that have achieved ignition with gain greater than 1 [1–3], advances in predictive capability of radiation-hydrodynamic codes [3,4] have played a critical role. The hohlraum size, wall material, gas fill, and laser power profile are chosen to provide an optimum time-dependent and spatially symmetric x-ray radiation drive. Despite these advances, simulations currently require “... artificial multipliers (less than unity) on the input laser power to the integrated simulations to match the measured in-flight symmetry, in-flight capsule velocity, and shock velocities along two lines of sight (pole and equator)” [3], and to match the timing of peak fusion energy production. Using drive multipliers implies simulations do not account for all input laser energy (“drive deficits”), which is measured to  $\sim 2\%$  accuracy [5]. This decade-long puzzle [4] affects ICF and other high-energy-density experiments [6,7].

Current laser power multipliers can reduce x-ray drive to match experiment, but they also reduce incident laser intensity, hampering accurate crossbeam energy transfer calculations [8] thereby compromising predictions of implosion shape. These power multipliers are believed to compensate for other inaccuracies in models affecting radiation drive and/or capsule response. Various explored hypotheses include laser decoupling due to specular reflection [9–11], wall-ablator or wall-gas mix [12], and wall properties [13,14]. Previously observed inaccuracies in modeling closure of the laser-entrance-hole (LEH) [15] have been resolved in more recent simulations that better describe LEH geometry [16,17]. To date, no hypothesis has definitively explained drive deficits.

Here we report a series of hohlraum science experiments aiming to isolate this problem, using specialized targets to examine radiation drive from the hohlraum wall and determine if x-ray emission is overpredicted. Recent upgrades to the x-ray emission diagnostic Dante [18] enabled these experiments, with measurement uncertainties reduced to 5% in

absolute total x-ray flux and incorporating a multilayer-mirror channel [19] for absolute flux between 2 and 4 keV with 9% accuracy [20]. Separately, in the “gold bubble” plasma produced where the outer laser beams heat the hohlraum, the electron temperature ( $T_e$ ) is monitored using Mn or Zn dopants [21,22]. The simultaneous collection of multiple measurements significantly constrains possible causes of drive deficits. The specialized targets (ViewFactor) [23] were first developed to study laser coupling in 0.96–1.6 mg/cc helium-filled hohlraums with “low foot” [24–26] and “high foot” [27–29] drives. ViewFactor targets are gold hohlraums with the upper 1/3 removed, providing an open end supplying unobscured views of the full extent of the interior wall (Fig. 1). In this work, ViewFactor targets enable examination of radiation drive for two current ICF designs, Hybrid E (HyE) [30–33] and SQN [34–39] which both use different helium fills (0.3 mg/cc), higher power, and shorter pulse shapes than previous ViewFactor experiments [23].

To give intuition into the x-ray energy production from the hohlraum wall, we describe the physics processes responsible for the partition of energy within the hohlraum. The incident laser power is converted into x rays with a conversion efficiency that depends on complicated processes such as inverse bremsstrahlung absorption, heat transport, laser-plasma interactions that can reflect a portion of the incident energy, and the x-ray emissivity in the conversion region. The x rays subsequently drive a radiation heat wave into the cooler, denser wall where most of the incident flux is reflected but some is absorbed. It has been shown that the wall loss depends on the heat capacity, absorption opacity, and radiation temperature [40,41]. Because the wall losses scale as the square root of the heat capacity, an underestimate in the heat capacity could decrease the total x-ray flux but would only slightly alter its spectral composition. An overestimate in the absorbed laser power would overestimate x-ray production in approximately a linear fashion. On the other hand, an overestimate in opacity and hence emissivity would both overestimate x-ray

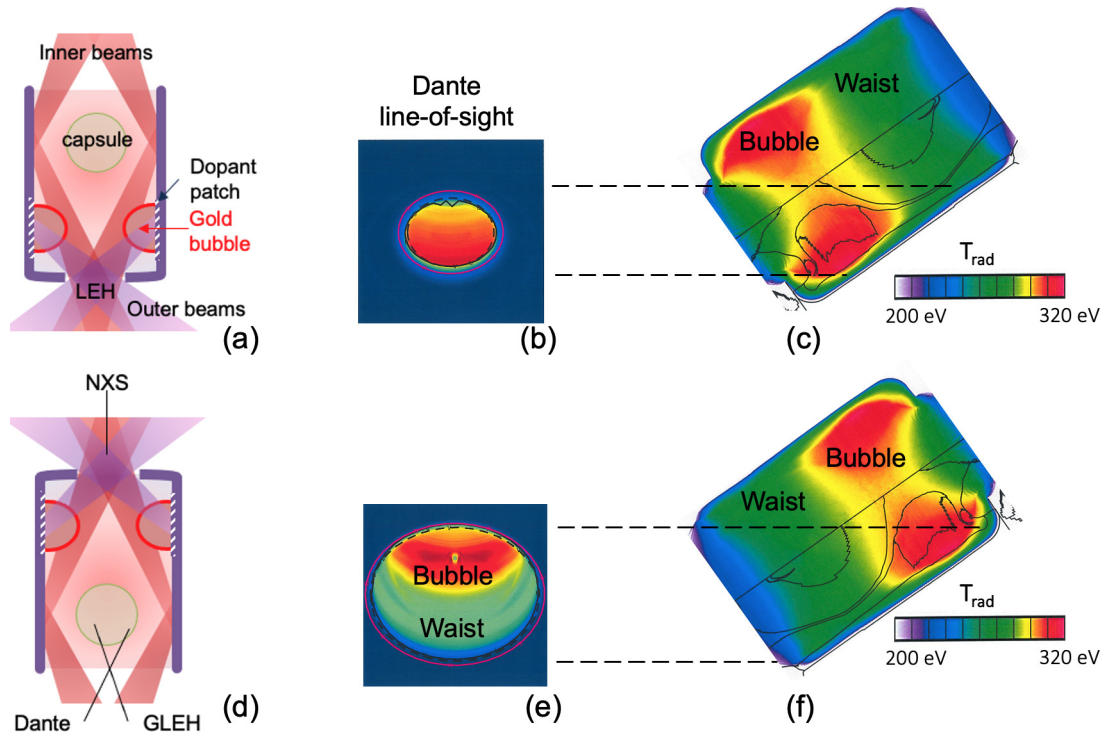


FIG. 1. Diagrams for the ViewFactor targets, diagnostics, and corresponding Dante views. (a) Target with LEH-end down where the LEH, dopant patch, and laser beams are labeled. The capsule is made of a CH shell (see main text for details). For this target, the NXS views the target through LEH while Dante and GLEH view the target from the open end. (b) The view of the Dante from the LEH end and the  $T_{rad}$  map (c) inside the target within Dante’s line of sight. The dark lines in the map indicate the material boundary in the simulation. (d) Target with open end down, and the view angle of the three main diagnostics. (e) The Dante view of target from the open end where the hotter bubble region is less dominant, as in the  $T_{rad}$  map (f).

conversion efficiency and underestimate wall loss. Further, because the opacity is a function of photon energy, it can also be used to explain a discrepancy between measured and simulated spectral composition of the x-ray flux [18].

The results reported here show that simulations (using the 2D radiation-hydrodynamics code LASNEX [42]) overpredict the total radiation drive, and more significantly the  $>1.8$  keV (“M band”) radiation. Using an opacity multiplier on M-band emissivity in the nonlocal thermodynamic equilibrium (NLTE) region results in much-improved agreement for both radiation drive and gold bubble temperatures inferred from K-shell spectroscopy of Mn or Zn dopants. Therefore, inaccuracies in atomic modeling of the NLTE gold plasma appear to account for most of the drive deficits between measured and simulated hohlraum x-ray flux.

Each gold target for the six ViewFactor experiments consisted of half of a subscale ignition hohlraum plus a 2-mm cylindrical extension without an LEH endcap (Fig. 1). Five shots used targets of 5.75 mm diameter, 7.07 mm length, and 3.37 mm LEH diameter; the sixth (N231026) was 5.4 mm diameter, 7.0 mm length, and 3.45 mm LEH diameter. Laser pulses are plotted in Fig. 2. The 5.75-mm-diameter targets were shot using HyE or extended HyE pulse shapes (SQN-like) with a more gradual rise (time extended  $\sim 1.5$  ns). The 5.4-mm-diameter target used the exact SQN pulse shape [34] from shot N230201-001. Rather than ignition capsules, 2-mm-diameter, 25- $\mu$ m-thick plastic shells were used, with holes so that the interior fill matches the hohlraum. Rapid

shell ablation enables unobscured wall views through the open end, while approximating the plasma conditions of full HyE or SQN hohlraums. The hohlraum is cooled to 32 K before the experiment. A band of 200-nm Au comixed with either Mn or Zn was placed in the hohlraum wall at the outer beam location. Figures 1(a) and 1(d) depict the “LEH-end” down and “open-end” down configurations, respectively. A pair of these configurations were shot using each laser pulse shape. For LEH-end down experiments, the target was driven using the NIF lower inner (23° and 30° polar angle, 32 beams) and outer (44° and 50°, 64 beams) beam cones, and the upper inner beam cone (150° and 157°, 32 beams), for a total of 128 beams [Fig. 1(a)]. The open-end down experiments used the mirror-image beam configuration: upper inner and outer cones, and the lower inner cone [Fig. 1(d)].

The primary diagnostic measures absolute x-ray flux using Dante, a time-resolved 18-channel filtered diode array soft x-ray spectrometer [18]. Dante views into the bottom of each target from 37.4° off the hohlraum axis. One channel (number 2) uses a multilayer-mirror [20] to record the absolute flux between 2 and 4 keV, which comprises over 90% of the  $>1.8$  keV M-band flux in a typical ICF experiment. The second key diagnostic is the NIF x-ray spectrometer (NXS) [43] viewing the target from the pole [Fig. 1(d)] to measure both time-resolved and time-integrated K-shell dopant emission from the gold bubble. The gated LEH diagnostic (GLEH) [44], an x-ray pinhole array imaging onto a ns-gated hCMOS sensor [45], measured LEH closure by viewing into

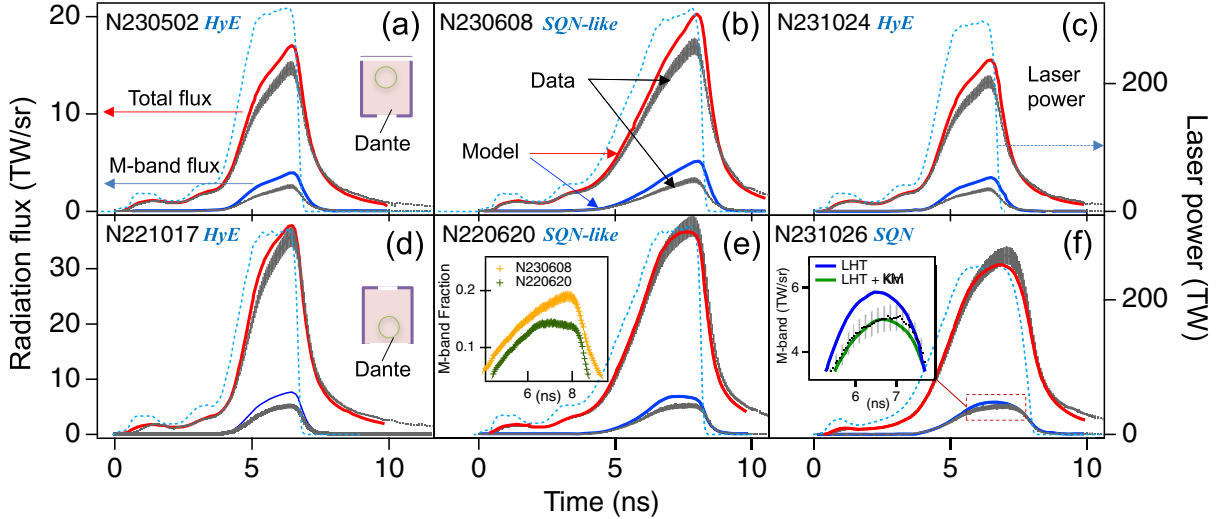


FIG. 2. Overview of the radiation flux measurement and simulation from six shots. The top row all had target with LEH end down [inset in (a)], and the bottom open end down [inset in (d)]. For each shot, the Dante total flux (upper grey trace) and  $>1.8$ -keV flux (lower grey trace) with linewidth as the uncertainty are plotted with the LHT simulations (total flux in red line,  $M$ -band flux in blue line); the laser pulse shape is plotted (cyan, dash line, right axis). Inset in (e): the fraction of  $M$  band over the total Dante flux; and inset in (f): an enlarged peak region of the  $M$ -band data and results from two models (LHT and LHT + KM).

the bottom of each target from  $18^\circ$  off the hohlraum axis [Fig. 1(d)].

Dante’s location is fixed, but changing target orientation from “LEH down” to “LEH up” gives it a different view of the hohlraum interior. Viewing through the LEH [Fig. 1(b)], Dante’s line of sight is limited to a smaller region dominated by outer beam-driven gold bubble [Fig. 1(c)]. But when Dante views through the open-end [Fig. 1(d)], its view [Fig. 1(e)] includes the entire hohlraum wall length [Fig. 1(f)] illuminated by inner and outer beams, but only a fraction of the bubble plasma region. These features unique to ViewFactor targets allow us to isolate the region responsible for drive deficits.

High quality Dante total and  $M$ -band ( $>1.8$  keV) flux time histories were recorded (Fig. 2) with  $\sim 280$ -eV peak radiation temperature ( $T_{\text{rad}}$ ) using either HyE, SQN-like, or SQN laser pulse shapes. In Fig. 2 the top (bottom) row show LEH-end down (open-end down) data with  $\sim 15$  TW/sr ( $\sim 35$  TW/sr) peak total flux. The two target orientations yield different flux amplitudes since, for open-end down, Dante sees a much larger, but cooler area than for LEH-end down. In addition, the ratio of  $M$  band to total radiation flux is higher when Dante measures through LEH end versus open end. This is illustrated in the inset of Fig. 2(e) for two shots that had the same SQN-like pulse shape with comparable laser power.

For each shot, the predicted flux is simulated using the baseline LASNEX Hohlraum Template (LHT) model [11,46], which models heat transport using a flux limiter  $f = 0.15$  [10,47,48]. Local thermodynamic equilibrium (LTE) opacity models are used for temperatures below 300 eV, and NLTE DCA models [49,50] for higher temperatures. Overall, the simulated total radiation flux shows closer agreement with data with a Dante view through open end ( $<10\%$ ) than a Dante view through LEH end ( $>10\%$ ). The discrepancy for the  $M$  band is larger (30–50%). Table I presents ratios of peak total and  $M$ -band flux between simulation and measurement.

Errors in simulated LEH closure are unlikely to explain this discrepancy, although inaccuracies in LEH closure modeling were earlier found responsible for some overprediction of the radiation drive [15]. Modeling improvements have since resulted in matching direct measurements of LEH size for a shot series using 0.3 mg/cc  $^4\text{He}$ -filled hohlraums [16]. Further, LEH closure was measured directly in the experiments reported here, and simulations agree with these measurements for all models [Fig. 3(d)].

To match simulations to the  $M$ -band flux measurement (Table I), we employ an opacity multiplier for gold  $M$  band (photon energy  $>1.8$  keV) radiation, as illustrated in the inset plot of Fig. 2(f) for one experiment (N231026). This choice is made because flux scales more strongly with opacity than heat capacity, and because of greater modeling uncertainty for gold  $M$ -band emissivity. The simulated radiative emission in this spectral region is predominantly produced by hot, low-density NLTE gold bubble plasma. The complex collisional-radiative calculations used in NLTE modeling of high- $Z$  elements require accurate representation of multiple atomic processes

TABLE I. Summary of experiments (column 1), target orientation and laser pulse shape (column 2), peak total flux ratio ( $R_{\text{peak}}^0$ ) between measurement and baseline simulation (column 3),  $M$ -band flux ratio ( $R_M^0$ ) (column 4), required  $M$ -band multiplier ( $k_M$ ) to match the  $M$ -band flux (column 5), and resulting peak total flux ratio ( $R_{\text{peak}}^1$ ) (column 6).

Expt.	Target/laser	$R_{\text{peak}}^0$	$R_M^0$	$k_M$	$R_{\text{peak}}^1$
N230502	LEH down/HyE	0.86	0.64	0.80	0.95
N231024	LEH down/HyE	0.85	0.65	0.81	0.95
N230608	LEH down/SQN-like	0.84	0.63	0.78	0.93
N221017	LEH up/HyE	0.94	0.76	0.88	0.99
N220620	LEH up/SQN-like	1.06	0.91	0.96	1.06
N231026	LEH up/SQN	1.05	0.87	0.90	1.06

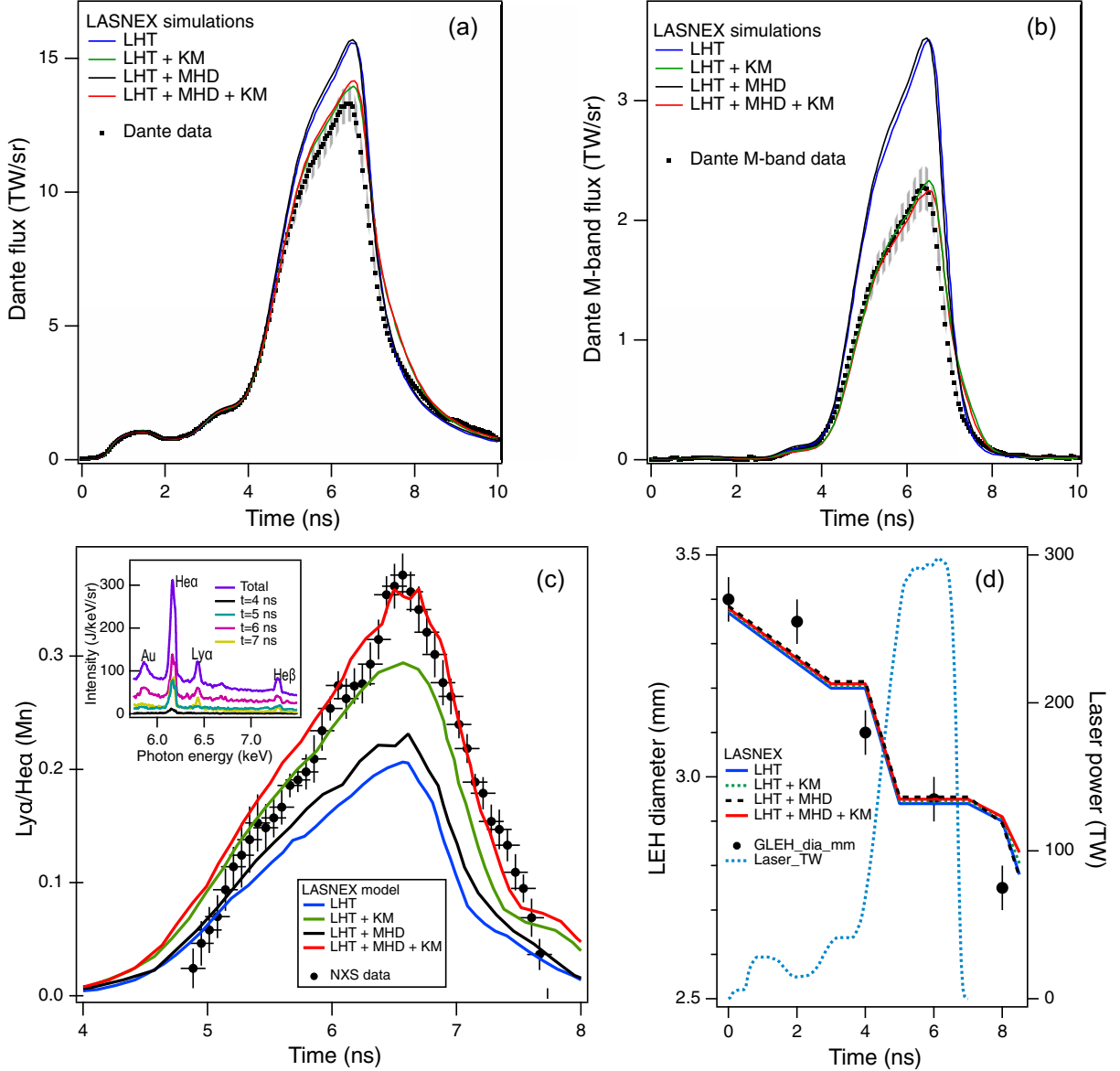


FIG. 3. The simulation results from four LASNEX models [1-LHT, 2-(LHT + KM), 3-(LHT + MHD) and 4-(LHT + MHD + KM)] are compared to measurement for N231024: (a) Dante total flux; (b) Dante  $M$  band; (c) dopant Mn  $K$ -shell line ratio with the inset showing the total spectrum and spectra for four times. The lines are labeled. (d) LEH diameter vs time from GLEH.

[51] and are believed to be less accurate than LTE models used to simulate thermal radiation [52]. Recent comparisons of NLTE calculations at similar densities and temperatures (with no radiation field) demonstrate large variations in  $M$ -band emission between different atomic models [53].

The use of a multiplier,  $\kappa_M$ , on the  $M$  band opacities mostly changes the emission in the bubble region, which is dominated by hotter NLTE plasmas relative to the cooler waist region (Fig. 1). For LEH-end down experiments, simulations using  $\kappa_M \sim 0.80$  could match measured Dante  $M$ -band flux and also improve the total flux comparison (Table I); when using  $\kappa_M$ , most of the simulated total Dante flux reduction arises from the  $M$ -band flux reduction. For experiments when the Dante view is through the open end, a  $\kappa_M$  closer to 1.0,  $\sim 0.9$ – $0.95$ , is needed to bring simulation into agreement with the data (Table I, last three rows). The difference in required

$\kappa_M$  reflects the plasma conditions in the emitting region visible to Dante (Fig. 1), with hotter plasma requiring more adjustment (lower  $\kappa_M$ ). The required  $\kappa_M$  appears to scale with the measured-vs-simulated flux ratio ( $R_M^0$ , column 4 in Table I) as  $\kappa_M \sim \sqrt{R_M^0}$ .

These comparisons were extended using simulations including an MHD (Magneto-Hydro-Dynamic) model [54,55] with and without opacity multipliers. In simulations, the MHD model affects neither the total nor  $M$ -band flux, consistent with prior work [56]. Figures 3(a) and 3(b) show N231024 [Fig. 2(c)] as an example: both models (blue and black traces) overpredict the radiation flux by about 18%. Only simulations with an opacity multiplier (red and green traces) could match the flux measurements within the error (required  $\kappa_M \sim 0.8$ ). However, including MHD in the baseline LHT model with and without the opacity multiplier has significant effects on

gold bubble plasma electron temperatures (up to 1 keV). This temperature increase occurs because self-generated azimuthal magnetic fields inhibit heat transport within the bubble [56]. In both models, opacity multipliers below unity also raise the temperature by reducing emitted radiation. Consequently, the electron temperature sensitive  $K$ -shell dopant (Mn)  $\text{Ly}\alpha/\text{He}\alpha$  line ratio [Fig. 3(c)] can be used [21,22] to discriminate between these models.

The time-resolved Mn x-ray spectra were recorded using NXS viewing from above the target [Fig. 1(d)]. The spectral energy coverage, 5.5–7.5 keV, encompassed the He-like and H-like Mn spectral lines [Fig. 3(c), inset]. The line ratio of  $\text{Ly}\alpha$  ( $1s - 2p$ ,  $^2S_{1/2} - ^2P_{3/2,1/2}$ ) and  $\text{He}\alpha$  ( $1s2 - 1s2p$ ,  $^1S_0 - ^1P_1$ ,  $^3P_1$ ) transitions is temperature sensitive as H-like ion populations, therefore  $\text{Ly}\alpha$  intensity, increase at higher temperature. Figure 3(c) shows measured and simulated line ratios versus time. In this comparison, the  $\text{He}\alpha$  complex flux includes contributions from unresolved Li-like satellite lines due to limited spectral resolution ( $\sim 50$  eV). During the laser power rise, the LHT model with  $k_M = 0.8$  follows the measurement, while at the peak, the best fit comes from the LHT + MHD model with  $k_M = 0.8$ . The latter has peak mass-weighted  $T_e \sim 4.7$  keV, versus  $\sim 3.8$  keV for the baseline LHT model (with  $k_M = 1$ ). Thus, these models show that an opacity multiplier combined with an MHD prescription later in time can match both the x-ray flux measurements and temperature measurements within the bubble.

Finally, Fig. 3(d) shows that all four models give similar fits to LEH closure measurements from GLEH, indicating the LEH closure is insensitive to the variations of the model. The agreement between the data and simulation is good at the peak laser power. There is a discrepancy in the LEH diameter of less than 2% at the early time when the radiation flux is low, and at late time when the laser is off. This comparison shows that LEH closure is an unlikely cause for the radiation flux discrepancies discussed here.

To verify this model, we have applied it to a separate set of NIF experiments where hohlraum targets started simple (with a large LEH but without an LEH membrane, gas fill, or capsule) and then incrementally added complexity, stepping towards an ignitionlike target. Similarly, the laser pulse was varied from a simple square pulse to a three-shock pulse. The simulated  $M$ -band flux was similarly 40–60% above the measurement. Using an opacity multiplier of 0.87, both the simulated peak Dante and  $M$ -band fluxes agree within measurement error. Furthermore, when applying this to the final integrated shot, the time of peak neutron production (bang

time) is shifted later by  $\sim 200$  ps, bringing simulated bang time within 110 ps of measurement. This much improved agreement with both radiation drive and capsule bang time indicates that the model is robust and applicable to additional types of targets.

It is not too surprising that  $M$ -band radiation is not simulated accurately causing the overprediction of total radiation flux. Comparisons among multiple models of calculated plasma ionization and emissivity for high- $Z$  elements, under conditions comparable to the hohlraum gold bubbles, consistently exhibit large variations [56]. Identifying and measuring these discrepancies in  $M$ -band radiation provides guidance for improving NLTE models used in simulations. The most critical and least certain atomic model parameters for ionization balance are the autoionization rates [51,57]. For a given charge state distribution, line emission depends strongly upon collisional excitation rates; measurements of selected transitions responsible for gold  $M$ -band radiation indicate significant overpredictions of those cross sections [58]. While simulations using modified rates can serve to identify computational sensitivities, focused experiments [59] should experimentally constrain updated NLTE models.

Separately, although we saw improvement using this model for an integrated implosion experiment, more study is needed to quantify the effects of this model on the capsule shock timing and compression trajectory for broader ICF experiments. Capsule implosion data should further constrain hypotheses for remaining disagreements between simulations and measurements, such as the capsule material equation-of-state, opacity etc.

In conclusion, a set of experiments using ViewFactor targets have revealed that the inaccuracy in the emission calculation for the gold  $M$  band is likely responsible for much, if not all, of the long-standing “drive deficits” for hohlraum simulations used for indirect drive ICF experiments. The common hohlraum model with MHD and  $\sim 20\%$  reduction in  $M$ -band opacity can bring the simulations into agreement with two independent measurements: the absolute radiation flux measurements (both total and  $M$  band) and hohlraum wall dopant spectroscopic line ratios. Such a model is applicable to other experiments that use high- $Z$  hohlraums as drivers for various high-energy-density experiments.

We are thankful for the useful discussions with Dr. E. Marley and Dr. R. Heeter. This work was performed under the auspices of the U.S. Department of Energy by LLNS, LLC, under Contract No. DE-AC52-07NA27344.

[1] H. Abu-Shawareb *et al.* (The Indirect Drive ICF Collaboration), *Phys. Rev. Lett.* **132**, 065102 (2024).  
 [2] O. A. Hurricane *et al.*, *Phys. Rev. Lett.* **132**, 065103 (2024).  
 [3] A. L. Kritcher *et al.*, *Phys. Rev. E* **109**, 025204 (2024).  
 [4] O. S. Jones *et al.*, *Phys. Plasmas* **19**, 056315 (2012).  
 [5] J.-M. Di Nicola *et al.*, (unpublished).  
 [6] C. C. Kuranz *et al.*, *Nat. Commun.* **9**, 1564 (2018).  
 [7] A. L. Kritcher *et al.*, *Nature (London)* **584**, 51 (2020).

[8] P. Michel *et al.*, *Phys. Rev. Lett.* **102**, 025004 (2009).  
 [9] N. Lemos *et al.*, *Phys. Plasmas* **29**, 092704 (2022).  
 [10] W. A. Farmer *et al.*, *Phys. Plasmas* **31**, 022705 (2024).  
 [11] O. S. Jones *et al.*, *Phys. Plasmas* **24**, 056312 (2017).  
 [12] P. Amendt, *Phys. Plasmas* **28**, 072701 (2021).  
 [13] M. Rubery, in *64th Annual Meeting of the APS Division of Plasma Physics* (2022), <https://meetings.aps.org/Meeting/DPP22/Session/PO04.1>.

- [14] W. A. Farmer, in *64th Annual Meeting of the APS Division of Plasma Physics* (2022), <https://meetings.aps.org/Meeting/DPP22/Session/PO04.2>.
- [15] M. B. Schneider *et al.*, *Phys. Plasmas* **22**, 122705 (2015).
- [16] H. Chen *et al.*, *Phys. Plasmas* **27**, 022702 (2020).
- [17] D. P. Higginson, D. J. Strozzi, D. Bailey, S. A. MacLaren, N. B. Meezan, S. C. Wilks, and G. Zimmerman, *Phys. Plasmas* **29**, 072714 (2022).
- [18] M. S. Rubery, G. E. Kemp, M. C. Jones, N. Pelepchan, W. C. Stolte, and J. Heinmiller, *Rev. Sci. Instrum.* **94**, 031101 (2023).
- [19] B. Emprin, Technical Report No. FRCEA-TH-7066, Institut d'Optique Graduate School, 2014.
- [20] M. S. Rubery *et al.*, *Rev. Sci. Instrum.* **93**, 113502 (2022).
- [21] M. A. Barrios *et al.*, *Phys. Plasmas* **23**, 056307 (2016).
- [22] M. A. Barrios *et al.*, *Phys. Rev. Lett.* **121**, 095002 (2018).
- [23] S. A. MacLaren *et al.*, *Phys. Rev. Lett.* **112**, 105003 (2014).
- [24] J. D. Lindl, *Phys. Plasmas* **2**, 3933 (1995).
- [25] J. D. Lindl *et al.*, *Phys. Plasmas* **21**, 129902 (2014).
- [26] S. W. Haan *et al.*, *Phys. Plasmas* **18**, 51001 (2011).
- [27] H.-S. Park *et al.*, *Phys. Rev. Lett.* **112**, 055001 (2014).
- [28] T. R. Dittrich *et al.*, *Phys. Rev. Lett.* **112**, 055002 (2014).
- [29] O. A. Hurricane *et al.*, *Nature (London)* **506**, 343 (2014).
- [30] O. A. Hurricane *et al.*, *Plasma Phys. Control. Fusion* **61**, 014033 (2019).
- [31] O. A. Hurricane *et al.*, *Phys. Plasmas* **26**, 052704 (2019).
- [32] A. L. Kritcher *et al.*, *Nat. Phys.* **18**, 251 (2022).
- [33] B. Zylstra *et al.*, *Phys. Rev. E* **106**, 025202 (2022).
- [34] S. Clark *et al.*, *Phys. Plasmas* **29**, 052710 (2022).
- [35] A. Do, C. R. Weber, E. L. Dewald, D. T. Casey, D. S. Clark, S. F. Khan, O. L. Landen, A. G. MacPhee, and V. A. Smalyuk, *Phys. Rev. Lett.* **129**, 215003 (2022).
- [36] C. R. Weber, D. S. Clark, D. T. Casey, G. N. Hall, O. Jones, O. Landen, A. Pak, and V. A. Smalyuk, *Phys. Rev. E* **108**, L023202 (2023).
- [37] A. Do *et al.*, *Phys. Plasmas* **30**, 112703 (2023).
- [38] R. Tommasini *et al.*, *Phys. Rev. Res.* **5**, L042034 (2023).
- [39] D. S. Clark, A. Allen, S. H. Baxamusa, J. Biener, M. M. Biener, T. Braun, S. Davidovits, L. Divol, W. A. Farmer, T. Fehrenbach, C. Kong, M. Millot, J. Milovich, A. Nikroo, R. C. Nora, A. E. Pak, M. S. Rubery, M. Stadermann, P. Sterne, C. R. Weber, and C. Wild, *Phys. Plasmas* **31**, 062706 (2024).
- [40] M. D. Rosen, Fundamentals of ICF Hohlräume, in *High Energy Laser Matter Interactions*, edited by D. A. Jaroszynski, R. Bingham, and R. A. Cairns, Lectures in the Scottish Universities Summer School in Physics, 2005 (CRC Press Boca Raton, FL, 2009), pp. 325–353.
- [41] J. H. Hammer and M. D. Rosen, *Phys. Plasmas* **10**, 1829 (2003).
- [42] G. B. Zimmerman and W. L. Kruer, Comments, *Plasma Phys. Controlled Fusion* **2**, 51 (1975).
- [43] F. Pérez *et al.*, *Rev. Sci. Instrum.* **85**, 11D613 (2014).
- [44] H. Chen *et al.*, *Rev. Sci. Instrum.* **89**, 10G103 (2018).
- [45] J. L. Porter, Q. Looker, and L. Claus, *Rev. Sci. Instrum.* **94**, 061101 (2023).
- [46] A. J. Strozzi, D. S. Bailey, P. Michel, L. Divol, S. M. Sepke, G. D. Kerbel, C. A. Thomas, J. E. Ralph, J. D. Moody, and M. B. Schneider, *Phys. Rev. Lett.* **118**, 025002 (2017).
- [47] W. A. Farmer, C. Bruulsema, G. F. Swadling, M. W. Sherlock, M. D. Rosen, W. Rozmus, D. H. Edgell, J. Katz, B. B. Pollock, and J. S. Ross, *Phys. Plasmas* **27**, 082701 (2020).
- [48] W. A. Farmer, M. D. Rosen, G. F. Swadling, C. Bruulsema, C. D. Harris, W. Rozmus, M. B. Schneider, M. W. Sherlock, D. H. Edgell, J. Katz, and J. S. Ross, *Phys. Plasmas* **28**, 032707 (2021).
- [49] H. A. Scott and S. B. Hansen, *High Energy Density Phys.* **6**, 39 (2010).
- [50] M. D. Rosen *et al.*, *High Energy Density Phys.* **7**, 180 (2011).
- [51] H. A. Scott, C. T. Whelan, and S. H. Glenzer, *High Energy Density Phys.* **7**, 371 (2011).
- [52] Y. Ralchenko, in *Modern Methods in Collisional-Radiative Modeling of Plasmas*, Springer Series on Atomic, Optical, and Plasma Physics Vol. 90, edited by Y. Ralchenko (Springer, Switzerland, 2016), Chap. 8.
- [53] Y. Ralchenko (personal communication).
- [54] W. A. Farmer, J. M. Koning, D. J. Strozzi, D. E. Hinkel, L. F. B. Hopkins, O. S. Jones, and M. D. Rosen, *Phys. Plasmas* **24**, 052703 (2017).
- [55] D. J. Strozzi, H. Sio, G. B. Zimmerman, J. D. Moody, C. R. Weber, B. Z. Djordjevic, C. A. Walsh, B. A. Hammel, B. B. Pollock, A. Povilus, J. P. Chittenden, and S. O'Neill (unpublished).
- [56] S. B. Hansen, H.-K. Chung, C. J. Fontes, Y. Ralchenko, H. A. Scott, and E. Stambulchik, *High Energy Density Phys.* **35**, 100693 (2020).
- [57] H.-K. Chung, C. Bowen, C. J. Fontes, S. B. Hansen, and Y. Ralchenko, *High Energy Density Phys.* **9**, 645 (2013).
- [58] M. J. May *et al.*, *AIP Conf. Proc.* **1811**, 190009 (2017).
- [59] E. Marley, in *The 2018 International Workshop on Radiative Properties of Hot Dense Matter* (Hamburg, Germany, 2018).